Seeded growth of HgTe nanocrystals for shape control and their use in narrow infrared electroluminescence

Yoann Prado, Junling Qu, Charlie Gréboval, Corentin Dabard, Prachi Rastogi, Audrey Chu, Adrien Khalili, Xiang Zhen Xu, Christophe Delerue, Sandrine Ithurria, et al.

Seeded growth of HgTe nanocrystals for shape control and their use in narrow infrared electroluminescence

Yoann Prado[1], Junling Qu[1], Charlie Gréboval[1], Corentin Dabard[1,2], Prachi Rastogi[1], Audrey Chu[1], Adrien Khalili[1], Xiang Zhen Xu[2], Christophe Delerue[3], Sandrine Ithurria[2], Emmanuel Lhuillier[1*]

[1] Sorbonne Université, CNRS, Institut des NanoSciences de Paris, INSP, F-75005 Paris, France.
[2] Laboratoire de Physique et d'Etude des Matériaux, ESPCI-Paris, PSL Research University, Sorbonne Université Univ Paris 06, CNRS UMR 8213, 10 rue Vauquelin 75005 Paris, France.
[3] Université de Lille, CNRS, Centrale Lille, ISEN, Université de Valenciennes, UMR 8520-IEMN, 59000 Lille, France

Abstract: HgTe colloidal nanocrystals (NCs) have become a promising building block for infrared optoelectronics. Despite their cubic zinc blende lattice, HgTe NCs tend to grow in a multipodic fashion, leading to poor shape and size control. Strategies to obtain HgTe NCs with well-controlled sizes and shapes remain limited and sometimes challenging to handle, increasing the need for a new growth process. Here, we explore a synthetic route via seeded growth. In this approach, the small HgTe seeds are nucleated in the first step, and they show narrow and bright photoluminescence with 75% quantum yield in the near infrared region. Once integrated into Light emitting diodes (LEDs), these seeds lead to devices with high radiance up to 20 $W \cdot Sr^{-1} \cdot m^{-2}$ and a long lifetime. Heating HgTe seeds formed at the early stage leads to the formation of sphere-shaped HgTe with tunable band edges from 2 to 4 µm. Last, the electronic transport tests conducted on sphere-shaped HgTe NC arrays reveals enhanced mobility and stronger temperature dependence than the multipodic shaped particles.

*To whom correspondence should be sent: el@insp.upmc.fr

Introduction

Infrared detection technologies have long been driven by epitaxially grown semiconductors, such as InSb, HgCdTe and quantum well-based heterostructures. Over recent years, colloidal narrow band gap nanocrystals[1–3] (NCs) have emerged as a possible low-cost alternative. Among the potential candidates, HgTe is, along with lead chalcogenides, one of the most promising materials. HgTe NCs cover a spectral range similar to that of bulk HgCdTe alloys, while their spectral tunability comes from quantum confinement instead of alloying. Thus, 10 years ago, the material challenge was to achieve large particles to reach extended shortwave infrared (SWIR)[4,5] and midwave infrared (MWIR) absorption.[6,7] A significant part of the research effort during the past decade has been focused on integrating HgTe NCs in devices to obtain gate control,[8–11] enhanced light-matter coupling[12–15] and imaging using focal plane arrays.[16–20] The material side has not been neglected,[21] and the most striking developments include the observation of intraband absorption in self-doped nanoparticles,[22,23] the growth of bright emitters in the SWIR region,[24,25] pushing absorption up to the THz range[26], shape control with 2D nanoplatelet growth,[27] large-scale syntheses (several grams) using liquid Hg as a precursor[28] and the demonstration of core-shell growth[29,30] to control nonradiative pathways.

Now that the colloidal growth of HgTe NCs has reached a mature level, it is possible to correlate the material structure with physical properties, as opposed to the former situation where surface traps were used to dominate all the physical properties. In particular, significant efforts have been dedicated to correlating the shape of the particles with the resulting properties. HgTe, in spite of its cubic lattice (*i.e.,* zinc blende structure), tends to form nonspherical particles. The exact shape of the HgTe particles has been revealed using electron tomography and appears to be tripods[31] for particle sizes of approximately 10 nm, which switches to tetrahedrons with well-defined facets for particle sizes of approximately 15 nm.[32] Coupling tomography with atomistic tight-binding simulations has demonstrated that the shape does not greatly affect wavefunction overlap (*i.e.,* the exciton binding energy) but can lead to a significant shift in the band-edge energy with respect to the sphere.[31]

Shen *et al.* reported a chemical strategy to grow monodisperse spherical HgTe NCs.[22] Such a rounded shape seems beneficial for the transport mobilities,[33] probably by enabling better packing of the NCs and more efficient ligand exchange at the price of an increased exciton linewidth.[34] To obtain spherical HgTe NCs, Shen *et al.* used a highly reactive Te precursor, bis(trimethylsilyl) telluride [22] ($(TMS)_2Te$), as opposed to more conventional tellurium complexed with trioctylphosphine. However, $(TMS)_2Te$ presents clear drawbacks, including a high cost, a relatively short lifetime and the need for full air-free handling. It thus is of the utmost interest to develop alternative strategies to grow sphere-shaped HgTe NCs. Here, we explore the possibility of obtaining spherical HgTe NCs using a seeded growth approach. The concept is clearly inspired by recent works from Zamkov's[35] group on CdSe NCs. They demonstrated the possibility of performing the dissolution recrystallization of small CdSe seeds while heating them in the presence of an amine and cadmium oleate. Here, we demonstrate a strategy to grow very small HgTe NCs with a band edge in the near IR region with very good photoluminescence (PL) responses and a high quantum yield (QY) up to 75%. We show that these seeds can be used to design light-emitting diodes (LEDs) presenting very high brightness (up to 20 $W \cdot Sr^{-1} \cdot m^{-2}$). In the second step, we apply the strategy developed by Zamkov's group[35] to HgTe, and we identify growth conditions that enable the transformation of these small seeds into sphere-shaped HgTe NCs with tunable band edges in the shortwave and midwave infrared region (from 2 to 4 µm exciton peaks). Using tight binding simulations, we reveal that the linewidth has clear homogeneous contribution. Finally, we probe the electronic transport and photoconductive properties of spherical HgTe NC arrays and confirm that they exhibit better photoconductive properties (higher mobilities, larger transistor on-off ratios, higher activation energies) than nonspherical particles.

Experimental section

Chemicals: Mercury chloride ($HgCl_2$, Sigma-Aldrich, 99%), mercury bromide ($HgBr_2$, Alfa Aesar), mercury iodide (HgI_2, Touzart & Matignon), and **mercury compounds are highly toxic. Handle them with special care.** Tellurium powder (Te, Sigma-Aldrich, 99.99%), lead oxide (PbO, Strem Chemicals, 99.999+%), hexamethyldisilathiane (TMS_2S, Sigma Aldrich, synthesis grade), zinc acetate dihydrate ($Zn(CH_3COO)_2$, Sigma, 99.999%), trioctylphosphine (TOP, Alfa, 90%), octadecene (ODE, Acros Organics, 90%), oleic acid (OA, Sigma, 90%), oleylamine (OLA, Acros, 80-90%), dodecanethiol (DDT, Sigma-Aldrich, 98%), trioctylamine (TOA, Aldrich), 1,2 ethanedithiol (EDT, Fluka, 98%), butylamine (Alpha 99%), potassium hydroxide (KOH, Sigma 90%), tetramethylammonium hydroxide pentahydrate (TMAOH, 98%, Alfa Aesar), ethanolamine (Aldrich, ≥98%), hydrochloric acid (HCl, Mieuxa, 25%), anhydrous absolute ethanol (VWR), methanol (VWR, >98%), isopropanol (IPA, VWR), hexane (VWR, 99%), octane (Carlo erba, 99%), acetonitrile (VWR, 99.9%), 2-mercaptoethanol (MPOH, Merck, >99%), N,N dimethylformamide (DMF, VWR), chloroform (VWR), chlorobenzene (VWR), tetrachloroethylene (TCE, VWR), toluene (VWR, 99.8%), dimethyl sulfoxide (DMSO, ≥99.9%, Sigma-Aldrich), and ethyl acetate (VMR) were used. All chemicals were used without further purification.

1 M TOP:Te precursor: Te powder (2.54 g) was mixed in 20 mL of TOP in a three-neck flask. The flask was kept under vacuum at room temperature for 5 min, and then, the temperature was raised to 100 °C. Furthermore, degassing of the flask was conducted for the next 20 min. The atmosphere was switched to nitrogen, and the temperature was raised to 275 °C. The solution was stirred until a clear orange coloration was obtained. The flask was cooled to room temperature, and the color changed to yellow. Finally, this solution was transferred to a nitrogen-filled glove box for storage.

Seed growth: In a 20 mL vial, 144 mg (0.4 mmol) of $HgBr_2$ was dissolved in 3.6 mL of oleylamine at room temperature in air. Then, under stirring, 0.4 mL of TOP:Te (1 M) was added. Next, the reaction was quenched by adding 3 mL of a solution of DDT in toluene (10% v/v). The content of the flask was transferred into a centrifuge tube, and MeOH was added. After centrifugation, the formed pellet was redispersed with toluene. The solution was precipitated a second time with absolute EtOH. The formed pellet was redispersed in toluene. At this step, the nanocrystals were centrifuged in pure toluene to eliminate the lamellar phase. The solid phase was discarded. The solution was precipitated a last time with MeOH, and the pellet was redispersed in toluene. We typically obtained 10 mg of dried powder from this synthesis.

Spherical shaped HgTe NC growth: In a 50 mL three-neck flask, 18 mL of oleylamine was degassed under vacuum and heated to 120 °C for 1 h. Then, the atmosphere was switched to N_2, and the temperature was set at 120 °C. Meanwhile, in a vial, 72 mg of $HgBr_2$ (0.2 mmol) was dissolved in 1.8 mL of OLA under sonication. Then, after degassing, the solution, 0.2 mL of TOP:Te (1 M), was added (t_w=0). Then, after a waiting time of t_w = 10 min, the solution was transferred to the syringe, and the content was quickly introduced into hot OLA (120 °C). The solution color quickly turned dark brown. After 3 min, a cold mixture (*i.e.,* freezer cooled) of 1 mL DDT in 2 mL of toluene was injected, and an ice bath was used to quickly decrease the temperature. The content of the flask was transferred to a centrifuge tube, and NCs were precipitated by adding methanol. After centrifugation, the formed pellet was redispersed in toluene. The solution was precipitated a second time with absolute ethanol and redispersed in toluene. At this step, the NCs were centrifuged in toluene to eliminate the lamellar phase. The solid phase was discarded, and the stable solution phase was transferred to a weighed centrifuge tube and finally precipitated using methanol. Again, the formed pellet (45 mg of dried powder was typically obtained) was redispersed in toluene.

Material characterization: For TEM imaging, a drop of diluted NC solution was cast on a copper grid covered with an amorphous carbon film. The grid was degassed overnight under secondary vacuum. A JEOL 2010F system was operated at 200 kV for the acquisition of images. For infrared

spectroscopy, we used a Fischer Nicolet iS50 system in attenuated total reflection (ATR) mode. The spectra are averaged over 32 acquisitions and have 4 cm^{-1} resolution.

Photoluminescence quantum yield (PLQY): The PLQY of HgTe NCs in solution was obtained by an Edinburgh Instrument spectrometer equipped with an integrating sphere. The samples were excited at 900 nm with a Xe lamp, and the photons were collected with an InGaAs detector cooled by liquid N_2. HgTe NCs were dispersed in tetrachloroethylene to decrease the absorption of the solvent. A series of solutions with optical densities from 0.014 to 0.084 at 900 nm were measured.

Tight binding simulations: We used the tight binding model of ref 36 to calculate the electronic structure of the HgTe NCs. Each Hg or Te atom is described by a double set of $sp^3d^5s^*$ orbitals, one for each spin orientation. Surfaces were saturated by pseudohydrogen atoms characterized by a single s orbital. Tight-binding parameters, *i.e*., on-site energies, nearest-neighbor hopping matrix elements and spin-orbit coupling terms, were determined to provide a very good description of the band structure of bulk HgTe (at 300 K). For all NCs, we calculated 60 (1200) conduction (valence) states, and we computed dipolar matrix elements between them as described in ref [36].

Results and discussion

To understand the need for a new synthesis of HgTe NCs, it is important to estimate the limitations of the current procedure. The method proposed by Keuleyan *et al* [37] is certainly the most commonly used for device integration. First, it is now established that the polydispersity of the obtained HgTe NCs is clearly reduced while growth is conducted under dilute conditions,[7] which increases solvent consumption and the associated cost. Second, in the hot injection method used for NC growth, the nucleation and growth steps are ideally uncoupled to obtain a single nucleation step. This can typically be obtained by the fast injection of the anion precursor into a solution containing cations, ligands and solvent. Part of the issue with the current procedure comes from the strong mixing of these two steps, as was already pointed out by Brennan *et al.*[38] in the early 90s. In Figure S1, we show that the slow injection of TOP:Te into the oleylamine and mercury solution does not lead to a broadened band edge feature with respect to that resulting from fast injection. By switching to a more reactive Te precursor, Shen *et al.* demonstrated that a better size distribution can be achieved[22].

Here, we used a different approach and grow sphere-shaped particles from a seeded synthesis approach. The concept has been explored recently for HgTe NC growth by Kershaw *et al*. while conducting growth in polar solvents[24]. In our case, we focused on growth in a nonpolar reaction medium typically made of an amine used as a coordinating solvent. The first step relates to seed growth. The reactivity of mercury compounds with Te is high, which enables the synthesis of HgTe NCs at fairly low temperatures (60-120 °C). At room temperature, the reaction rate is reduced, but nucleation still occurs. We preserved the same reaction scheme (mercury halides + TOP:Te in oleylamine, see Figure 1a) as that used by Keuleyan *et al.*[37] while conducting the reaction at room temperature. This reaction is followed by UV-vis spectrometry. It clearly shows that a reaction occurs with exciton formation at approximately 900 nm (see Figure 1b), followed by an increase in its magnitude without presenting an energy shift with time. The trend is observed with all halides (Cl, Br and I); see Figure 1c and S2. In the following, we focus on mercury bromide,[39] as it leads to the slowest kinetic growth at room temperature, enabling a higher degree of control. Moreover, chloride salts present the drawback of lower solubility in OLA, while bromide and iodine are fully soluble. The reaction rated appears to be fasten by the presence of water, see figure S3-4.

It is possible to extract these seeds from the reaction medium by quenching the mixture with a long chain thiol (DDT). The quenched seeds present a band edge reaching 1100 nm, suggesting that surface thiols are involved in charge delocalization. The approximate size of these seeds is found to be approximately 2.7 nm according to TEM and X-ray diffraction (see Figure 1e and S6). This corresponds to a cluster containing 300 atoms. Such a small cluster is consistent with the formation

of magic-size clusters, which would explain why we do not observe a band edge shift during the reaction. For the sake of comparison, a band edge at 900 nm is similar to that observed with 3 monolayer nanoplatelets whose sizes are approximately 1.1 nm.[40]

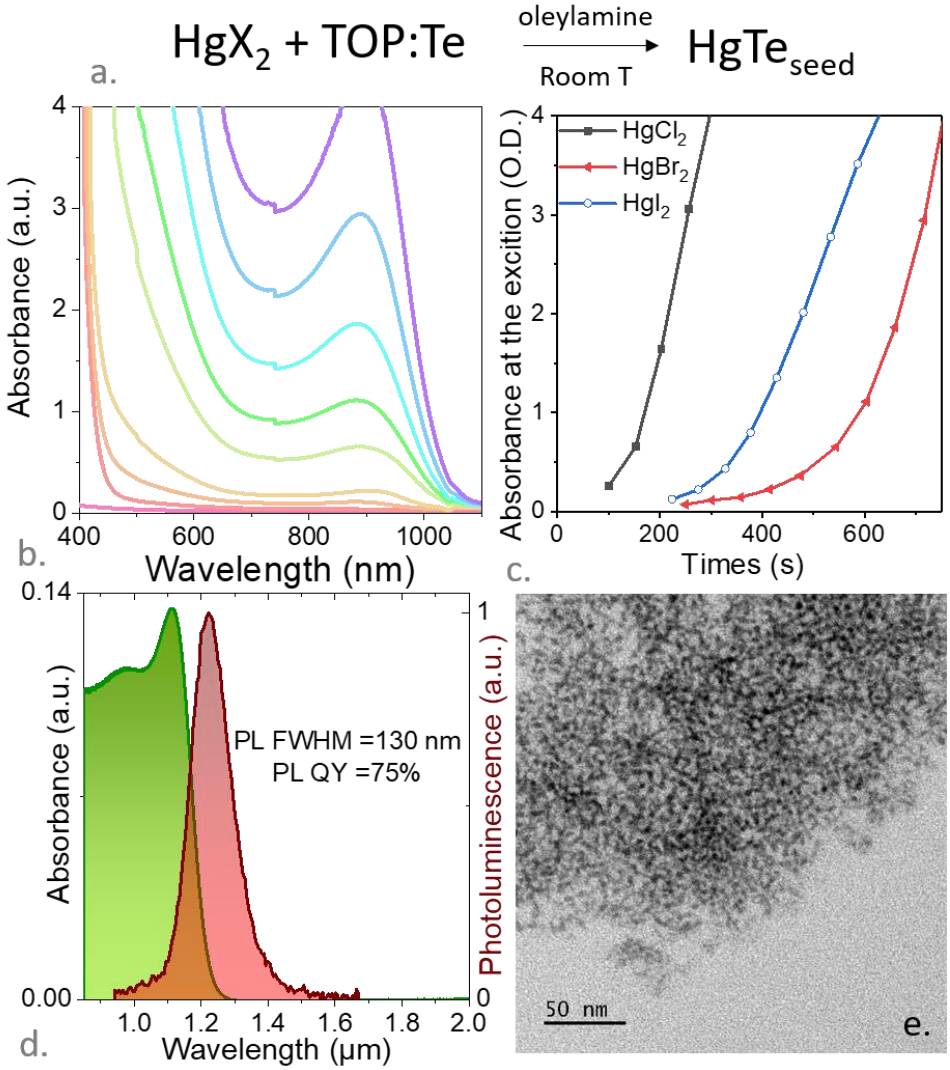

Figure 1 a. Chemical reaction conducted to obtain small HgTe seeds. b. UV-vis absorption spectra for a mixture of $HgBr_2$ and TOP:Te (1:1 Hg:Te ratio) in oleylamine at room temperature, leading to HgTe seeds at different times after mixing the Hg and Te precursors. c. Absorption at the exciton as a function of time for the seeds, while the mercury halides are $HgCl_2$, $HgBr_2$ and HgI_2. d. Absorption and photoluminescence spectra of the quenched HgTe seeds ($HgBr_2$ was used as a precursor, the Hg:Te ratio was 1:1, and the reaction proceeded at room temperature). e. Transmission electron microscopy image of the HgTe seeds.

Interestingly, these seeds also show PL, as shown in Figure 1d. The latter is narrow and presents a quality factor (the peak emission energy divided by the full width at half maximum) of 10, while the quality factor is 7.5 for the HgTe NCs obtained from the procedure of Geiregat *et al.*[41] with a similar PL wavelength; see figure S7. In addition, the PLQY reached 75%, while with the previous strategy, the PL efficiency was below 50%.[42] This shows that the seeds on their own are actually of the greatest interest for LED design. Paradoxically, minimal efforts have been dedicated to HgTe NC-based LEDs.[42–44] Recently, Qu *et al.*,[45] using a strategy initially developed for PbS NCs,[46] demonstrated that HgTe NCs can be efficient radiative recombination centers once they are integrated into a solar cell-like diode structure. Here, we use the same structure based on a glass/ITO/ZnO/ZnO-HgTe/PbS/Au stack (see Figure 2a) while using small HgTe seeds as the emitting material. In this structure, gold/p-type PbS is used as a hole injector, while ITO/ZnO is used as an electron injector. The band gap of the PbS layer is chosen to be larger than that of HgTe so that the PbS layer does not behave as a recombination center.[45] The emitting layer is a bulk

heterojunction where electron conduction is ensured by ZnO and hole conduction is ensured by HgTe. To make this layer conductive while preserving the PL signal, the initial long ligands are replaced by dipping the film into a solution of $HgCl_2$ (see the SI). This LED leads to bright electroluminescence (EL), as shown in Figure 2b. The EL signal appears to be redshifted compared to the PL signal shown in Figure 1d, which is the result of absorption, and the PL spectra shift with time, even if the particles are stored in solution (see Figure S14). The turn-on voltage of the LED is ≈0.6 V (Figure 2e) corresponding to subband-gap (≈890 meV) operation. The maximum external quantum efficiency (EQE) at roll-off reaches 0.25%, see Figure 2d. This value remains modest compared to the values (reaching 8% EQE) achieved using PbS.[47] However, this diode presents limited efficiency droop while operated with a high driving current. As a result, high radiance (>13 $W{\cdot}Sr^{-1}{\cdot}m^{-2}$ can be achieved during 80 h of operation; see Figure 2c. This matches the brightness of PbS NC-based LEDs operating in the SWIR region, and this LED outperforms previously reported devices based on HgTe NCs.[42–44] Under lower current operating conditions (corresponding to a radiance of 2-5 $W{\cdot}Sr^{-1}{\cdot}m^{-2}$), we do not observe a decay in the performance but rather observe a slow increase in the brightness after a week (>200 h) of continuous operation in air.

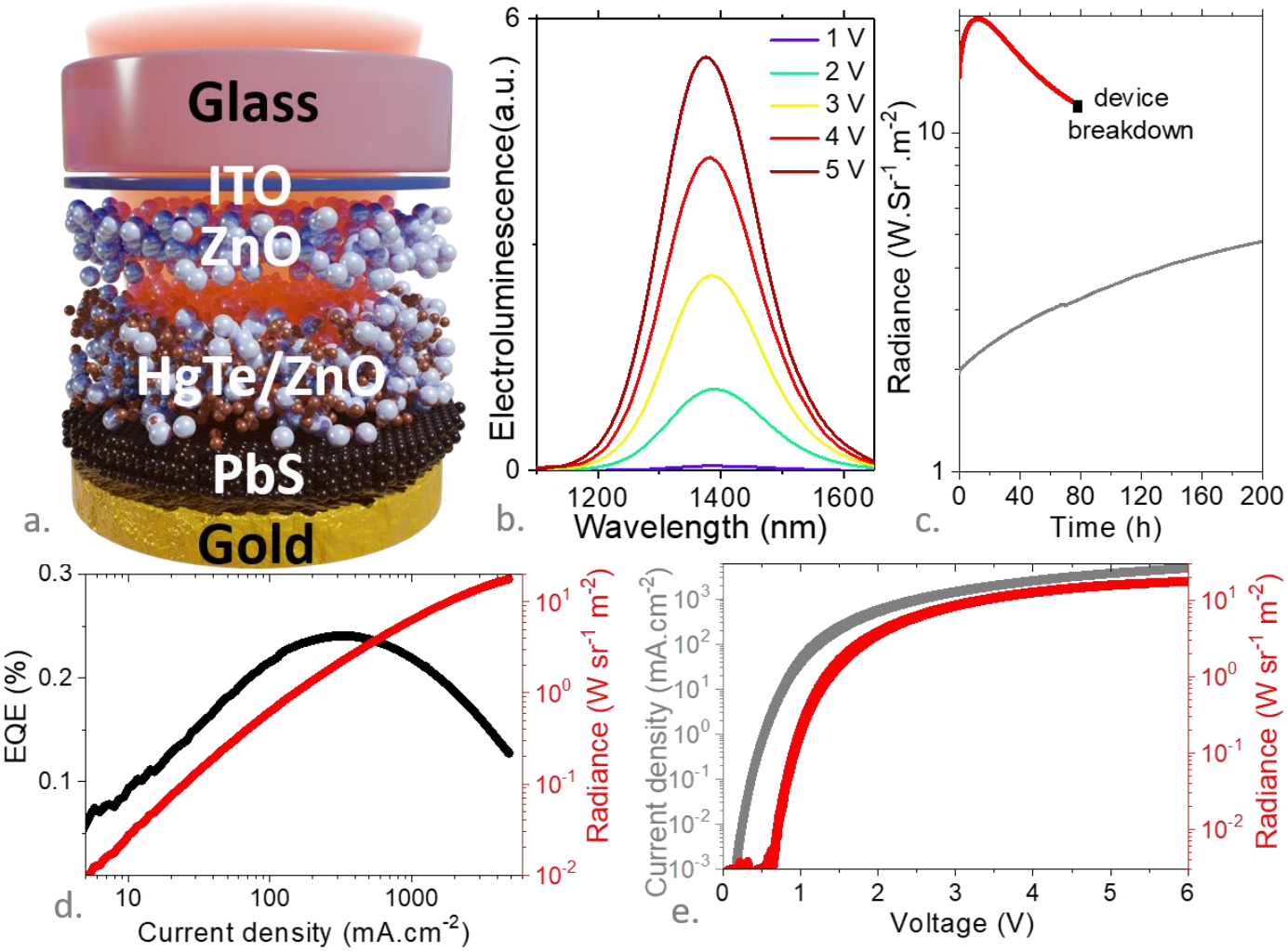

Figure 2 a. Scheme of a diode made of ITO/ZnO/ZnO-HgTe seeds/PbS/Au emitting SWIR light. b. Electroluminescence spectra of the diode depicted in part a operated under different biases. c. Radiance as a function of time for a diode operated under constant current conditions (I= 3 mA for the 2 $W{\cdot}Sr^{-}{\cdot}m^{-2}$ (gray) initial radiance and I=29 mA for the 15 $W{\cdot}Sr^{-1}{\cdot}m^{-2}$ initial radiance (red)). d. External quantum efficiency (EQE) and radiance as a function of the driving current. e. Current density and radiance as a function of the applied bias.

To further explore the versatility of the HgTe seeds, we used the seeds formed at the early stage to obtain spherical HgTe NCs with absorption in the SWIR and MWIR regions (see Figure 3a). To do so, a solution of mercury bromide in OLA was mixed with TOP:Te under nitrogen at room temperature for 10 min, leading to the formation of seeds, but at an early stage, the solution was still yellow after 10 min of reaction. The process appears to be dependent on moisture (wet atmosphere accelerates the reaction); see Figure S3-4. Such moisture dependence may further reinforce the hypothesis of a magic-size cluster intermediate, since the latter is known to be stabilized by protic molecules.[48] The yellow colored solution was then injected in hot (100-150 °C) oleylamine. The solution quickly became dark, confirming the growth of infrared absorbing NCs. This observation is further confirmed by the absorption spectra (Figure 3b-c). Furthermore, X-ray diffraction confirms that the material is HgTe with a zinc blende structure (see Figure S8). TEM observations (Figure 3d-f) show a quasi-spherical shape, with no interparticle aggregation. The largest particles clearly display some facets (Figure 3f) but are neither branched nor aggregated. The yield of the reaction (45 mg of QDs per 0.2 mmol of $HgBr_2$) is similar to that obtained with Keuleyan's procedure[37] (39 mg of QDs per 0.2 mmol of $HgCl_2$). The fact that our process leads to sphere-shaped objects contrasts with the idea that phosphines were responsible for the tripod shape previously obtained.

While the synthesis is inspired by the procedure developed by Cassidi *et al.*[35] for CdSe, the mechanisms of the reaction appear to be quite different. In the case of CdSe, the seeds were cleaned and later injected into hot oleylamine, and growth occurred through a dissolution recrystallization process. In the case of HgTe, the growth of the seed in the presence of monomers leads to larger particles. In addition, the lack of these monomers prevents the growth of sphere-shaped NCs (see Figure S12). Thus, even if we cannot fully exclude the partial dissolution of the seeds, the free monomers are clearly involved in the growth of spherical NCs.

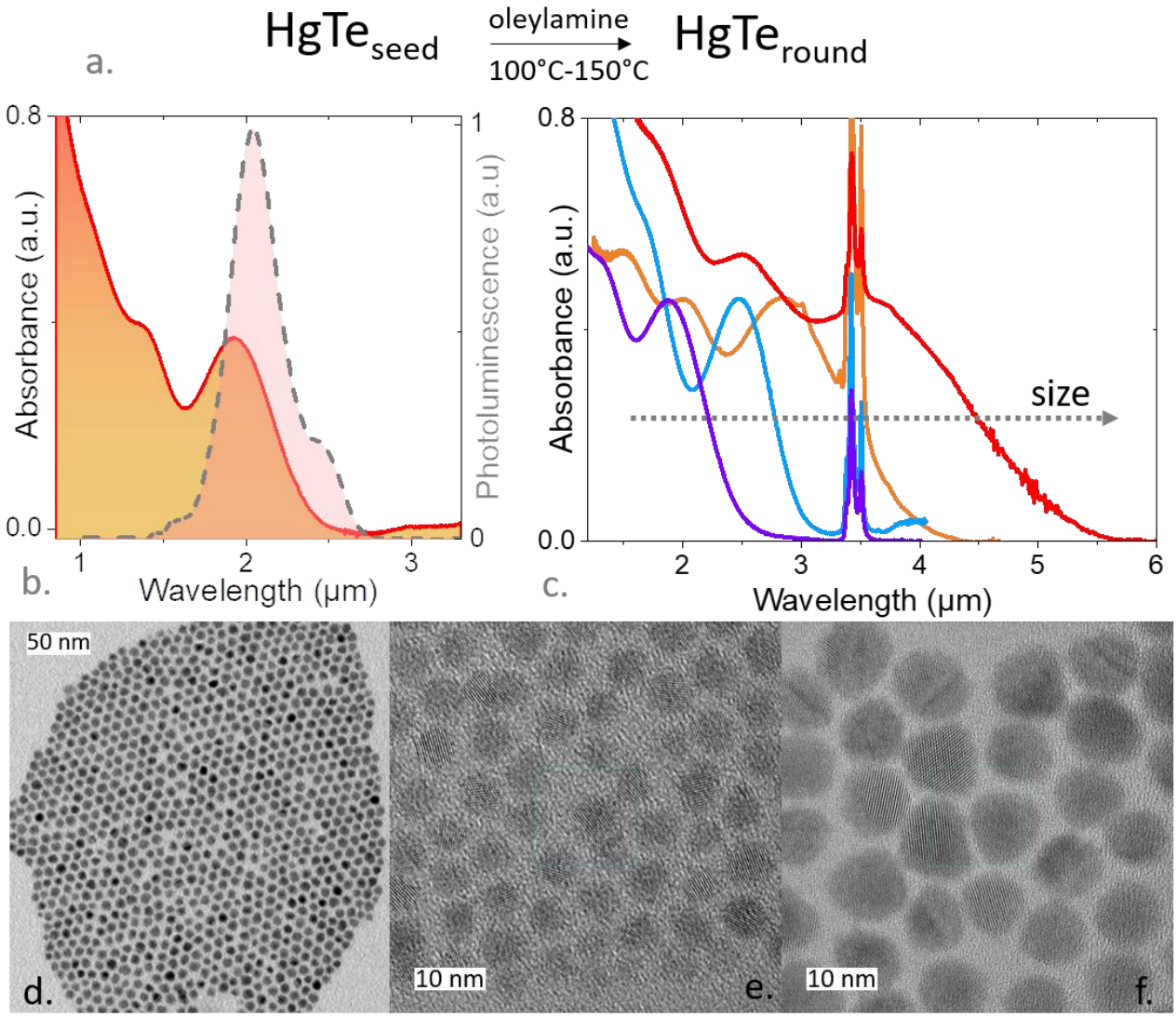

Figure 3 a. Chemical reaction is conducted to obtain round HgTe NCs. b. Absorbance and photoluminescence spectra of a solution made of round HgTe NCs (Hg:Te=2:1; 30 s of reaction at 110 °C). c. Absorbance spectra of round HgTe NCs of various sizes. The smallest particles are grown at 110 °C, and the largest are grown at 150 °C. d. Transmission electron microscopy image of round HgTe NCs with a band edge at 2.5 µm. e. High-resolution image of the population imaged in d. f. High-resolution transmission electron microscopy image of sphere-shaped HgTe NCs with a band edge at 4 µm.

The peak band edge can be tuned from 2 to 4 µm (Figure 3c and S10) using the following parameters: (*i*) the temperature of the reaction (the higher the temperature is, the larger the particle; this is the main parameter driving the final size; see Figure S10a), (*ii*) the duration of the reaction (the longer the duration is, the larger the particle; see Figure S10b), and (*iii*) the Hg:Te stoichiometry (excess Hg tends to reduce the particle size; see Figure S5 and S10c). Scale-up of the reaction at a constant concentration is possible, but we observe that an increase in the concentration above a factor of 3 leads to the loss of the spherical shape (see Figure S11).

The spectra (Figure 3b-c) appear to be more structured (*i.e.,* the observation of several bumps) than the one obtained from tripod-shaped particles (see Figure S1). In particular, it is possible to correlate the sphere shape to the presence of a dip in the spectrum following the first exciton (see Figure 4a). However, the linewidth of the first excitonic feature is much broader than that achieved with PbSe, another traditional infrared material or even with tripod HgTe NCs (see Figure 4a). This broad linewidth is also observed from PL measurements (see Figure 3b). Hence, the full width at half maximum is 352 nm for emission at 2.04 µm, corresponding to Q=5.8. This value is indeed smaller (*i.e.,* corresponds to a broader PL signal) than the value obtained from the tripod NCs, Q=7.7.[49] On

the other hand, this value is larger than the value obtained from the synthesis based on $(TMS)_2Te$, where Q is approximately 4.1.[22]

The absorption spectrum is then fitted using a multiGaussian approach to highlight the different transitions occurring in the nanoparticles (see Figure 4b). Three main contributions are clearly visible and correspond to the transition from the valence band to the $1S_e$, $1P_e$ and $1D_e$ states of the conduction band. Note from this fit that the energy difference between the $1P_e$ and $1S_e$ states is approximately 0.25 eV (≈2000 cm^{-1}). The infrared spectrum in this energy range (Figure S13) does not show intraband peaks; thus, we can exclude that the NCs are doped.

To further unveil the electronic structure of these HgTe sphere-shaped NCs, we perform electronic structure simulations using a tight binding approach;[36] see Figure 4c. The band edge appears to be composed of two contributions. This may explain the presence of a small feature in the low-energy part of the PL spectrum, even though the presence of a trap state cannot be fully excluded.[41] This result is also consistent with a recent observation by Zhang *et al.*[34] who observed a dual feature band edge in sphere-shaped HgTe NCs. Simulations also confirm that the density of states is sparse (Figure 4c) at an energy just above the band edge, which explains the observation of the dip in the absorption spectrum after the first feature (see Figure 4a).

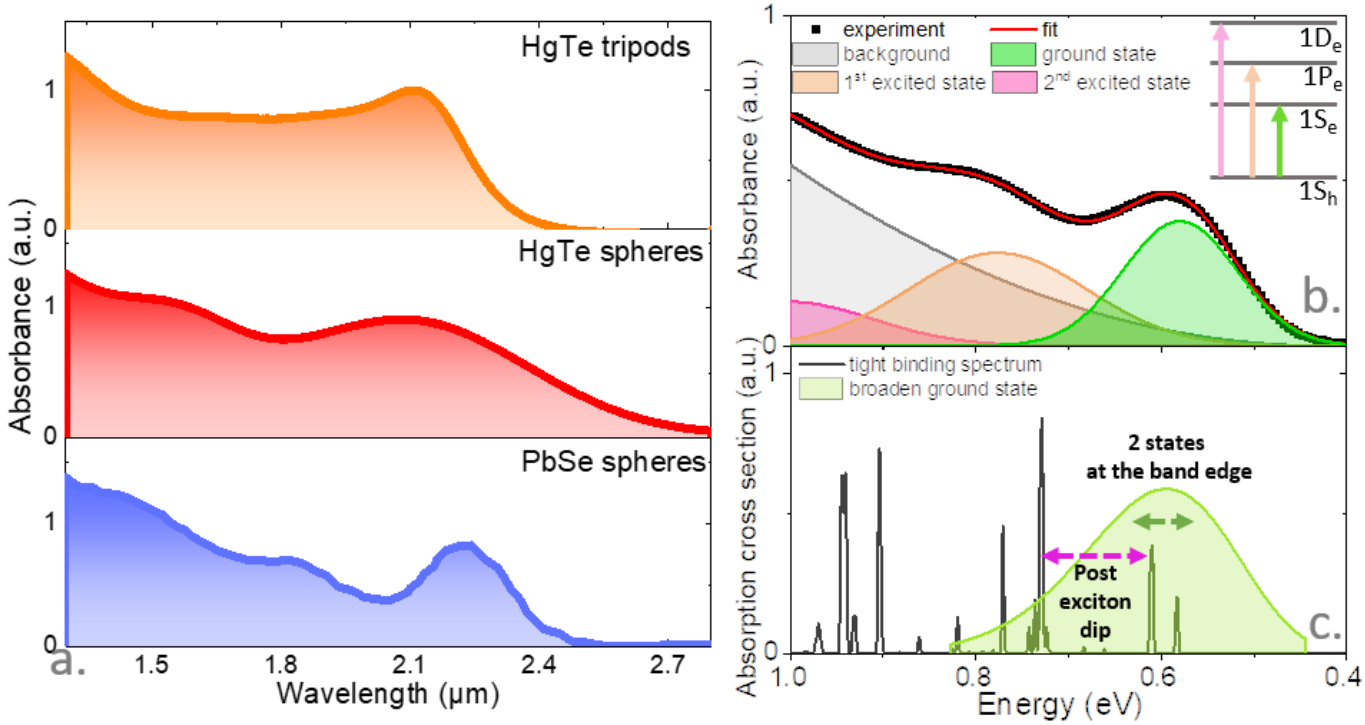

Figure 4 a. Absorbance spectra of tripod-shaped HgTe and spherical HgTe and PbSe NCs. b. Absorbance spectrum of spherical HgTe NCs and its multiGaussian fit, showing the different transitions occurring between valance and conduction bands. A parabolic background is used to fit the data. The inset is a sketch of the electronic spectrum, and the colored arrows correspond to the transition corresponding to the different transitions observed in the spectrum. c. Simulated absorbance of single sphere-shaped HgTe NCs (5.25 nm in size) leading to a band edge similar to the experimental data shown in part a. To compare the simulation with the experimental data, the peaks are first broadened with a 1.2 nm FWHM to account for homogeneous broadening, and then, we account for the particle size distribution as determined from TEM.

Thus far, we have demonstrated that shape control is possible, even using TOP:Te as a precursor. The following probes whether the physical properties of the obtained sphere-shaped NCs resulting from seeded growth match those of the spheres obtained using $(TMS)_2Te$. In particular, the sphere shape has led to enhanced carrier mobility.[33]

We then processed sphere- and tripod-shaped NCs with a band edge at 2.5 µm into an ink and deposited it onto interdigitated electrodes. The latter was then used as the channel of a field-effect transistor whose gate can either be an electrolyte or a dielectric (SiO_2). At room temperature, we focused on electrolyte gating since this method is associated with a high capacitance. This enables the good tunability of the current. At low temperature (below 280 K),[11] ions froze in the polymer matrix, and the gate effect was lost. In this case, we switched to a dielectric gate. The capacitance decreased but was consistent with low-temperature use.

The transistor transfer curves present an ambipolar nature, as shown in Figure 5a, with both hole and electron conduction. The neutrality point lies in both cases under a negative gate bias, suggesting inherent *n*-doping. This observation is consistent with previous photoemission measurements performed on the material, revealing a Fermi level in the upper part of the band gap.[50] Qualitatively, doping appears independent of the shape. On the other hand, the current modulation is much higher with the spheres (almost 3 orders of magnitude, whereas it was only one for tripods); see Figure 5a. In particular, the sharper slopes suggest higher mobilities for the film made of spheres (μ^e_{sphere} =3.8μ^e_{tripod}, and μ^h_{sphere}=3.5μ^h_{tripod}), which is consistent with previous reports based on synthesis relying on TMS_2Te.[33] We also notice that with spheres, the current at the minimum of conduction is also reduced, which suggests that the thermally activated carrier density is also lower and that the Fermi level might be deeper within the band gap. The temperature dependence of the current supports this observation; see Figure 5b. The spheres present a stronger temperature dependence, and the activation energy of the current in the vicinity of room temperature is 214 meV, quite close to the half band gap value ($E_G/2$≈250 meV), whereas the activation energy is approximately 120 meV for the tripods. The mobility of the film μ^e_{sphere} is found to be approximately 2x10^{-2} cm^2·V^{-1}s^{-1} close to room temperature and drops by two orders of magnitude at 50 K, see Figure 5c and S15.

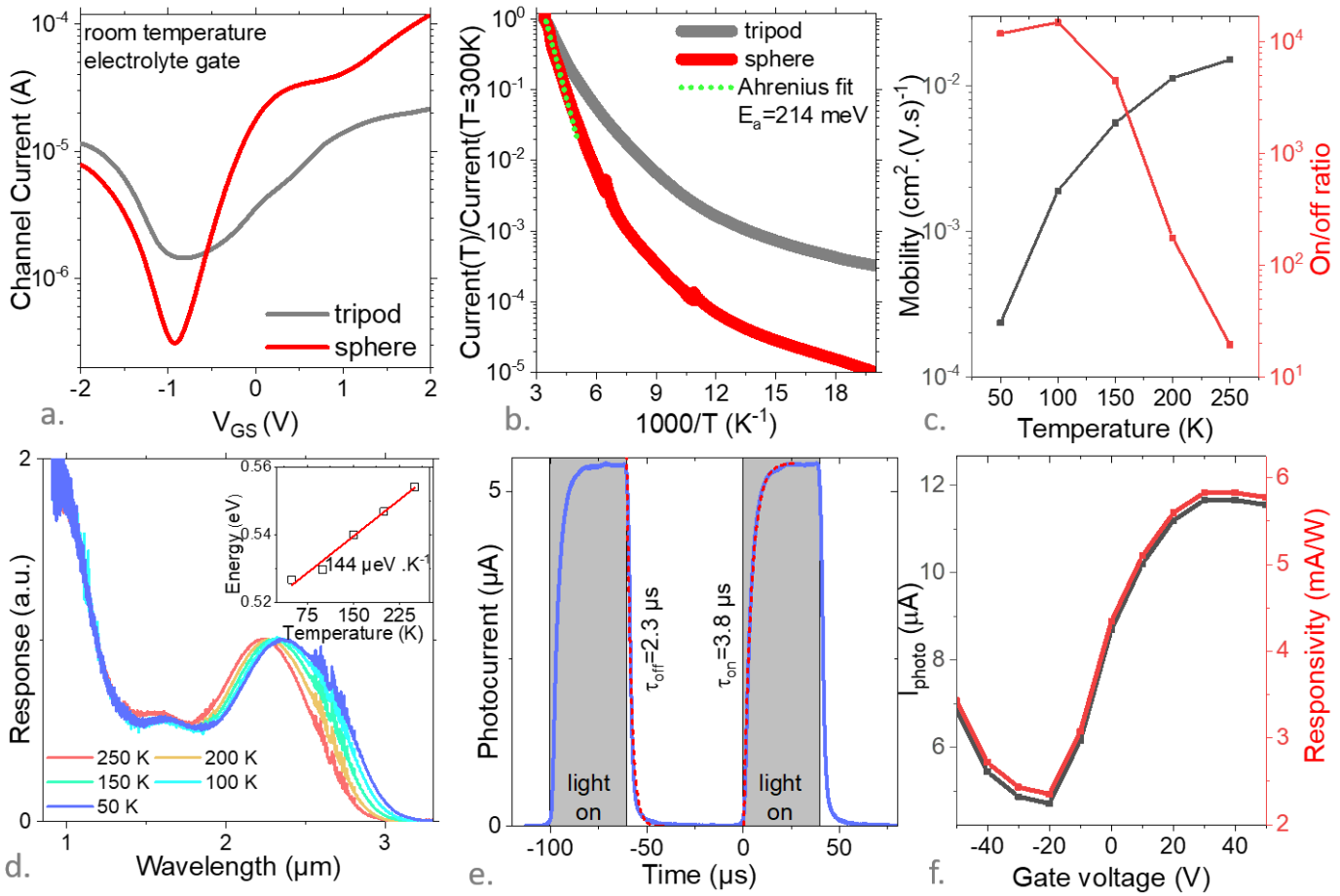

Figure 5 a. Transfer curves (drain current as a function of gate bias) obtained for thin films made of sphere-shaped and tripod-shaped HgTe NCs with the same surface chemistry (mercaptoethanol-$HgCl_2$). The gate is made of an electrolyte, and the measurement is conducted at room temperature. b. Current as a function of temperature for thin films made of round and tripod-shaped HgTe NCs. c. Mobility and current on/off ratio for a thin film made of round HgTe NCs. d. Photocurrent spectra

of a thin film made of round HgTe NCs at various temperatures. The inset shows the energy of the exciton as a function of temperature. e. Photocurrent as a function of time while the sample is illuminated by a pulse of light at 1.55 µm. f. Photocurrent and responsivity as a function of gate bias (SiO_2 gate here). For e and f, the measurements are conducted at 250 K. For all data, the applied drain source bias is 0.5 V.

To finish, we probed the photoconductive properties of such sphere-shaped HgTe NC arrays (see Figure 5d-f). Contrary to the tripods for which after ligand exchange, the photocurrent spectrum becomes featureless, the spheres maintain the characteristic of the absorption spectrum, with a clear exciton followed by a noticeable dip (see Figure 5d). As the temperature decreases, the photocurrent is redshifted; see the inset of Figure 5d. The value of dE_G/dT is found to be 144 µeV·K^{-1}, which is clearly smaller than the value obtained for tripods (190±20 µeV·K^{-1}).[51,52] We observe that the fast time response of the material is preserved in the case of spheres with turn-on and off times on the order of 2-4 µs (see Figure 5e), which is close to the experimental setup limitation. Finally, we show that gate bias can be used to control the magnitude of the photocurrent over a factor of 3; see Figure 5f. This observation is mostly interesting for operating the device in a situation that maximizes the photocurrent to the dark current ratio, since the latter is more dramatically tuned (a factor of 10 at 250 K, Figure S15) than the photocurrent (a factor of 3, see Figure 5e). Finally, the detectivity has been determined to be 10^8 Jones at room temperature (see Figure S16), making it worth integrating the material into a more complex diode geometry in the near future.

Conclusion

We demonstrate a novel synthetic path for the growth of HgTe NCs using a seeded growth approach. Room temperature-grown seeds present a sharp absorption and photoluminescence signal in the shortwave infrared region, with a PLQY reaching 75%. Once integrated into LEDs, these seeds lead to bright (>15 W ·Sr^{-1}·m^{-2}) electroluminescence and stable performance. Once the seeds are heated in oleylamine, they behave as nucleation centers for the additional monomers and lead to spherical-shaped HgTe NCs with tunable band edges between 2 and 4 µm. Our strategy offers an easy handling synthesis for the growth of sphere-shaped HgTe NCs with an excellent yield. Electronic transport within an array of sphere-shaped HgTe NCs reveals higher mobility and stronger temperature dependence than that achieved within branched-shaped particles, suggesting fewer traps within the bandgap. Last, this material is compatible with high responsivity and fast time responses, which is of utmost interest for future integration into focal plane arrays.

ASSOCIATED CONTENT

Supporting Information includes additional material characterizations, procedures to fabricate and characterize the LEDs and procedures to fabricate field effect transistors and characterize electronic transport.

COMPETING INTEREST

The authors declare no competing financial interests.

ACKNOWLEDGEMENTS

The project is supported by ERC starting grants blackQD (grant n° 756225) and Ne2Dem (grant n° 853049). We acknowledge the use of clean-room facilities at the “Centrale de Proximité Paris-Centre”. This work has been supported by Region Ile-de-France in the framework of DIM Nano-K

(grant dopQD). This work was supported by French state funds managed by the ANR within the Investissements d'Avenir programme under reference ANR-11-IDEX-0004-02 and, more specifically, within the framework of the Cluster of Excellence MATISSE and by grants IPER-Nano2, Copin (ANR-19-CE24-0022), Frontal (ANR-19-CE09-0017), Graskop (ANR-19-CE09-0026) and NITQuantum. JQ thanks the Chinese Scholarship Council for PhD funding, while AC thanks Agence Innovation Defense. We thank Jasmine Zhang for marginal involvement in the project.

REFERENCES

(1) McDonald, S. A.; Konstantatos, G.; Zhang, S.; Cyr, P. W.; Klem, E. J. D.; Levina, L.; Sargent, E. H. Solution-processed PbS quantum dot infrared photodetectors and photovoltaics. *Nat. Mater.* **2005**, *4*, 138–142.

(2) Lu, H.; Carroll, G. M.; Neale, N. R.; Beard, M. C. Infrared quantum dots: Progress, challenges, and opportunities. *ACS Nano* **2019**, *13*, 939–953.

(3) Hafiz, S. Bin; Scimeca, M.; Sahu, A.; Ko, D. K. Colloidal quantum dots for thermal infrared sensing and imaging. *Nano Converg.* **2019**, *6*, 7.

(4) Böberl, M.; Kovalenko, M. V.; Gamerith, S.; List, E. J. W.; Heiss, W. Inkjet-Printed Nanocrystal Photodetectors Operating up to 3 μm Wavelengths. *Adv. Mater.* **2007**, *19*, 3574–3578.

(5) Kovalenko, M. V; Kaufmann, E.; Pachinger, D.; Roither, J.; Huber, M.; Stangl, J.; Hesser, G.; Schäffler, F.; Heiss, W. Colloidal HgTe Nanocrystals with Widely Tunable Narrow Band Gap Energies: From Telecommunications to Molecular Vibrations Maksym. *J. Am. Chem. Soc.* **2006**, *128*, 3516–3517.

(6) Keuleyan, S.; Lhuillier, E.; Brajuskovic, V.; Guyot-Sionnest, P. Mid-infrared HgTe colloidal quantum dot photodetectors. *Nat. Photonics* **2011**, *5*, 489–493.

(7) Keuleyan, S. E.; Guyot-Sionnest, P.; Delerue, C.; Allan, G. Mercury Telluride Colloidal Quantum Dots: Electronic Structure, Size-Dependent Spectra, and Photocurrent Detection up to 12 μm. *ACS Nano* **2014**, *8*, 8676–8682.

(8) Chen, M.; Lu, H.; Abdelazim, N. M.; Zhu, Y.; Wang, Z.; Ren, W.; Kershaw, S. V; Rogach, A. L.; Zhao, N. Mercury Telluride Quantum Dot Based Phototransistor Enabling High-Sensitivity Room-Temperature Photodetection at 2000 nm. *ACS Nano* **2017**, *11*, 5614–5622.

(9) Dong, Y.; Chen, M.; Yiu, W. K.; Zhu, Q.; Zhou, G.; Kershaw, S. V; Ke, N.; Wong, C. P.; Rogach, A. L.; Zhao, N. Solution Processed Hybrid Polymer: HgTe Quantum Dot Phototransistor with High Sensitivity and Fast Infrared Response up to 2400 nm at Room Temperature. *Adv. Sci.* **2020**, *7*, 2000068.

(10) Noumbé, U. N.; Gréboval, C.; Livache, C.; Chu, A.; Majjad, H.; Parra López, L. E.; Mouafo, L. D. N.; Doudin, B.; Berciaud, S.; Chaste, J.; Ouerghi, A.; Lhuillier, E.; Dayen, J.-F. Reconfigurable 2D/0D p–n Graphene/HgTe Nanocrystal Heterostructure for Infrared Detection. *ACS Nano* **2020**, *14*, 4567–4576.

(11) Gréboval, C.; Noumbe, U.; Goubet, N.; Livache, C.; Ramade, J.; Qu, J.; Chu, A.; Martinez, B.; Prado, Y.; Ithurria, S.; Ouerghi, A.; Aubin, H.; Dayen, J.-F.; Lhuillier, E. Field-Effect Transistor and Photo-Transistor of Narrow-Band-Gap Nanocrystal Arrays Using Ionic Glasses. *Nano Lett.* **2019**, *19*, 3981–3986.

(12) Sergeev, A. A.; Pavlov, D. V; Kuchmizhak, A. A.; Lapine, M. V; Yiu, W. K.; Dong, Y.; Ke, N.; Juodkazis, S.; Zhao, N.; Kershaw, S. V; Rogach, A. L. Tailoring spontaneous infrared emission of HgTe quantum dots with laser-printed plasmonic arrays. *Light Sci. Appl.* **2020**, *9*, 16.

(13) Chen, M.; Shao, L.; Kershaw, S. V; Yu, H.; Wang, J.; Rogach, A. L.; Zhao, N. Photocurrent Enhancement of HgTe Quantum Dot Photodiodes by Plasmonic Gold Nanorod Structures. *ACS Nano* **2014**, *8*, 8208–8216.

(14) Tang, X.; Ackerman, M. M.; Guyot-Sionnest, P. Thermal Imaging with Plasmon Resonance Enhanced HgTe Colloidal Quantum Dot Photovoltaic Devices. *ACS Nano* **2018**, *12*, 7362–7370.

(15) Chu, A.; Gréboval, C.; Goubet, N.; Martinez, B.; Livache, C.; Qu, J.; Rastogi, P.; Bresciani, F. A.; Prado, Y.; Suffit, S.; Ithurria, S.; Vincent, G.; Lhuillier, E. Near Unity Absorption in Nanocrystal Based Short Wave Infrared Photodetectors Using Guided Mode Resonators.

ACS Photonics **2019**, *6*, 2553–2561.
(16) Chu, A.; Martinez, B.; Ferré, S.; Noguier, V.; Gréboval, C.; Livache, C.; Qu, J.; Prado, Y.; Casaretto, N.; Goubet, N.; Cruguel, H.; Dudy, L.; Silly, M. G.; Vincent, G.; Lhuillier, E. HgTe Nanocrystals for SWIR Detection and Their Integration up to the Focal Plane Array. *ACS Appl. Mater. Interfaces* **2019**, *11*, 33116–33123.
(17) Buurma, C.; Pimpinella, R. E.; Ciani, A. J.; Feldman, J. S.; Grein, C. H.; Guyot-Sionnest, P. MWIR imaging with low cost colloidal quantum dot films. *SPIE* **2016**, *9933*, 993303.
(18) Ciani, A. J.; Pimpinella, R. E.; Grein, C. H.; Guyot-Sionnest, P. Colloidal quantum dots for low-cost MWIR imaging. *SPIE* **2016**, *9819*, 333–341.
(19) Greboval, C.; Ferre, S.; Noguier, V.; Chu, A.; Qu, J.; Chee, S.-S.; Vincent, G.; Lhuillier, E. Infrared narrow band gap nanocrystals: recent progresses relative to imaging and active detection. 30th january 2020, *arXiv:2001.11554* **2020**, (accessed 2021-02-23).
(20) Chatterjee, A.; Pendyala, N. B.; Jagtap, A.; Koteswara Rao, K. S. R. Uncooled mid-wave infrared focal plane array using band gap engineered mercury cadmium telluride quantum dot coated silicon roic. *e-Journal Surf. Sci. Nanotechnol.* **2019**, *17*, 95–100.
(21) Green, M.; Mirzai, H. Synthetic routes to mercury chalcogenide quantum dots. *J. Mater. Chem. C* **2018**, *6*, 5097–5112.
(22) Shen, G.; Chen, M.; Guyot-Sionnest, P. Synthesis of Nonaggregating HgTe Colloidal Quantum Dots and the Emergence of Air-Stable n-Doping. *J. Phys. Chem. Lett.* **2017**, *8*, 2224–2228.
(23) Wang, H.; Lhuillier, E.; Yu, Q.; Zimmers, A.; Dubertret, B.; Ulysse, C.; Aubin, H. Transport in a Single Self-Doped Nanocrystal. *ACS Nano* **2017**, *11*, 1222–1229.
(24) Kershaw, S. V.; Yiu, W. K.; Sergeev, A.; Rogach, A. L. Development of Synthetic Methods to Grow Long-Wavelength Infrared-Emitting HgTe Quantum Dots in Dimethylformamide. *Chem. Mater.* **2020**, *32*, 3930–3943.
(25) Rogach, A.; Kershaw, S.; Burt, M.; Harrison, M.; Kornowski, A.; Eychmüller, A.; Weller, H. Colloidally Prepared HgTe Nanocrystals with Strong Room-Temperature Infrared Luminescence *Adv. Mater.* **1999**, *11*, 552-555.
(26) Goubet, N.; Jagtap, A.; Livache, C.; Martinez, B.; Portalès, H.; Xu, X. Z.; Lobo, R. P. S. M.; Dubertret, B.; Lhuillier, E. Terahertz HgTe Nanocrystals: Beyond Confinement. *J. Am. Chem. Soc.* **2018**, *140*, 5033–5036.
(27) Izquierdo, E.; Robin, A.; Keuleyan, S.; Lequeux, N.; Lhuillier, E.; Ithurria, S. Strongly Confined HgTe 2D Nanoplatelets as Narrow Near-Infrared Emitters. *J. Am. Chem. Soc.* **2016**, *138*, 10496–10501.
(28) Goubet, N.; Thomas, M.; Gréboval, C.; Chu, A.; Qu, J.; Rastogi, P.; Chee, S. S.; Goyal, M.; Zhang, Y.; Xu, X. Z.; Cabailh, G.; Ithurria, S.; Lhuillier, E. Near- To Long-Wave-Infrared Mercury Chalcogenide Nanocrystals from Liquid Mercury. *J. Phys. Chem. C* **2020**, *124*, 8423–8430.
(29) Sagar, L. K.; Walravens, W.; Maes, J.; Geiregat, P.; Hens, Z. HgSe/CdE (E = S, Se) Core/Shell Nanocrystals by Colloidal Atomic Layer Deposition. *J. Phys. Chem. C* **2017**, *121*, 13816–13822.
(30) Shen, G.; Guyot-Sionnest, P. HgTe/CdTe and HgSe/CdX (X = S, Se, and Te) Core/Shell Mid-Infrared Quantum Dots. *Chem. Mater.* **2019**, *31*, 286–293.
(31) Chee, S.; Gréboval, C.; Magalhaes, D. V.; Ramade, J.; Chu, A.; Qu, J.; Rastogi, P.; Khalili, A.; Dang, T. H.; Dabard, C.; Prado, Y.; Chaste, J.; Rosticher, M.; Bals, S.; Delerue, C.; Lhuillier, E.; Correlating Structure and Detection Properties in HgTe Nanocrystal Films. **2021**, *Submitted*.
(32) Gréboval, C.; Chu, A.; Magalhaes, D. V.; Ramade, J.; Junling Qu; Rastogi, P.; Khalili, A.; Chee, S.-S.; Aubin, H.; Vincent, G.; Bals, S.; Delerue, C.; Lhuillier, E. Ferroelectric Gating of Narrow Band-Gap Nanocrystal Arrays with Enhanced Light Matter Coupling. *ACS Photonics* **2021**, *8, 259–268*.
(33) Chen, M.; Lan, X.; Tang, X.; Wang, Y.; Hudson, M. H.; Talapin, D. V.; Guyot-Sionnest, P. High Carrier Mobility in HgTe Quantum Dot Solids Improves Mid-IR Photodetectors. *ACS Photonics* **2019**, *6*, 2358–2365.
(34) Zhang, H.; Guyot-Sionnest, P. Shape-Controlled HgTe Colloidal Quantum Dots and Reduced

Spin-Orbit Splitting in the Tetrahedral Shape. *J. Phys. Chem. Lett.* **2020**, *11*, 6860–6866.
(35) Cassidy, J.; Ellison, C.; Bettinger, J.; Yang, M.; Moroz, P.; Zamkov, M. Enabling Narrow Emission Line Widths in Colloidal Nanocrystals through Coalescence Growth. *Chem. Mater.* **2020**, *32*, 7524–7534.
(36) Allan, G.; Delerue, C. Tight-binding calculations of the optical properties of HgTe nanocrystals. *Phys. Rev. B* **2012**, *86*, 165437.
(37) Keuleyan, S.; Lhuillier, E.; Guyot-Sionnest, P. Synthesis of colloidal HgTe quantum dots for narrow mid-IR emission and detection. *J. Am. Chem. Soc.* **2011**, *133*, 16422–16424.
(38) Brennan, J. G.; Siegrist, T.; Carroll, P. J.; Stuczynski, S. M.; Reynders, P.; Brus, L. E.; Steigerwald, M. L. Bulk and nanostructure Group II-VI compounds from molecular organometallic precursors. *Chem. Mater.* **1990**, *2*, 403–409.
(39) Green, M.; Wakefield, G.; Dobson, P. J. A simple metalorganic route to organically passivated mercury telluride nanocrystals. *J. Mater. Chem.* **2003**, *13*, 1076–1078.
(40) Izquierdo, E.; Robin, A.; Keuleyan, S.; Lequeux, N.; Lhuillier, E.; Ithurria, S. Strongly Confined HgTe 2D Nanoplatelets as Narrow Near-Infrared Emitters. *J. Am. Chem. Soc.* **2016**, *138*, 10496–10501.
(41) Geiregat, P.; Houtepen, A. J.; Sagar, L. K.; Infante, I.; Zapata, F.; Grigel, V.; Allan, G.; Delerue, C.; Van Thourhout, D.; Hens, Z. Continuous-wave infrared optical gain and amplified spontaneous emission at ultralow threshold by colloidal HgTe quantum dots. *Nat. Mater.* **2018**, *17*, 35–41.
(42) Qu, J.; Rastogi, P.; Greboval, C.; Lagarde, D.; Chu, A.; Dabard, C.; Khalili, A.; Cruguel, H.; Robert, C.; Xu, X.; Ithurria, S.; Silly, M.; Ferré, S.; Marie, X.; Lhuillier, E. Electroluminescence from HgTe Nanocrystals and Its Use for Active Imaging. *Nano Lett.* **2020**, *20*, 6185–6190.
(43) O'Connor, É.; O'Riordan, A.; Doyle, H.; Moynihan, S.; Cuddihy, A.; Redmond, G. Near-infrared electroluminescent devices based on colloidal HgTe quantum dot arrays. *Appl. Phys. Lett.* **2005**, *86*, 201114.
(44) Koktysh, D. S.; Gaponik, N.; Reufer, M.; Crewett, J.; Scherf, U.; Eychmüller, A.; Lupton, J. M.; Rogach, A. L.; Feldmann, J. Near-Infrared Electroluminescence from HgTe Nanocrystals. *ChemPhysChem* **2004**, *5*, 1435–1438.
(45) Qu, J.; Rastogi, P.; Gréboval, C.; Lagarde, D.; Chu, A.; Dabard, C.; Khalili, A.; Cruguel, H.; Robert, C.; Xu, X. Z.; Ithurria, S.; Silly, M. G.; Ferré, S.; Marie, X.; Lhuillier, E. Electroluminescence from HgTe Nanocrystals and Its Use for Active Imaging. *Nano Lett.* **2020**, *20*, 6185–6190.
(46) Pradhan, S.; Di Stasio, F.; Bi, Y.; Gupta, S.; Christodoulou, S.; Stavrinadis, A.; Konstantatos, G. High-efficiency colloidal quantum dot infrared light-emitting diodes via engineering at the supra-nanocrystalline level. *Nat. Nanotechnol.* **2019**, *14*, 72–79.
(47) Pradhan, S.; Dalmases, M.; Baspinar, A. B.; Konstantatos, G. Highly Efficient, Bright, and Stable Colloidal Quantum Dot Short-Wave Infrared Light-Emitting Diodes. *Adv. Funct. Mater.* **2020**, *30*, 200445.
(48) Kirkwood, N.; Boldt, K. Protic additives determine the pathway of CdSe nanocrystal growth. *Nanoscale* **2018**, *10*, 18238–18248.
(49) Keuleyan, S.; Kohler, J.; Guyot-Sionnest, P. Photoluminescence of Mid-Infrared HgTe Colloidal Quantum Dots. *J. Phys. Chem. C* **2014**, *118*, 2749–2753.
(50) Jagtap, A.; Martinez, B.; Goubet, N.; Chu, A.; Livache, C.; Gréboval, C.; Ramade, J.; Amelot, D.; Trousset, P.; Triboulin, A.; Ithurria, S.; Silly, M. G.; Dubertret, B.; Lhuillier, E. Design of a Unipolar Barrier for a Nanocrystal-Based Short-Wave Infrared Photodiode. *ACS Photonics* **2018**, *5*, 4569–4576.
(51) Lhuillier, E.; Keuleyan, S.; Guyot-Sionnest, P. Erratum: Optical properties of HgTe colloidal quantum dots. *Nanotechnology* **2014**, *23*, 1757051.
(52) Moghaddam, N.; Gréboval, C.; Qu, J.; Chu, A.; Rastogi, P.; Livache, C.; Khalili, A.; Xu, X. Z.; Baptiste, B.; Klotz, S.; Fishman, G.; Capitani, F.; Ithurria, S.; Sauvage, S.; Lhuillier, E. The Strong Confinement Regime in HgTe Two-Dimensional Nanoplatelets. *J. Phys. Chem. C* **2020**, *124*, 23460–23468.

TOC graphic

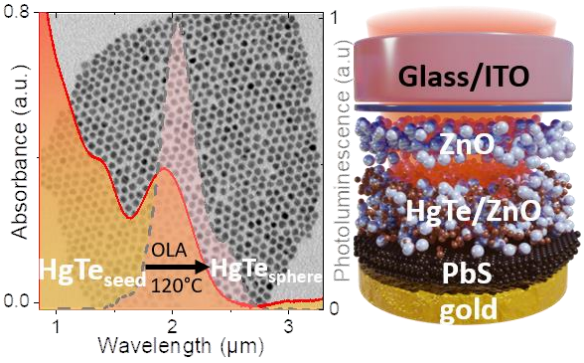
0.8
0.0
Absorbance (a.u.)
1
0
Photoluminescence (a.u)
1
2
3
Wavelength (μm)
HgTe seed
OLA
120°C
HgTe sphere
Glass/ITO
ZnO
HgTe/ZnO
PbS
gold